

Article

Research on a Measurement Method for Middle-Infrared Radiation Characteristics of Aircraft

Xuan Deng ^{1,2} , Yueming Wang ^{1,2,*} , Guicheng Han ¹ and Tianru Xue ^{1,2}

¹ Shanghai Institute of Technical Physics, Chinese Academy of Sciences, Shanghai 200083, China; dengxuan@mail.sitp.ac.cn (X.D.); hgc@mail.sitp.ac.cn (G.H.); xuetianru@mail.sitp.ac.cn (T.X.)

² University of Chinese Academy of Sciences, Beijing 100049, China

* Correspondence: wangym@mail.sitp.ac.cn

Abstract: Aiming at the problem wherein temperature inversion accuracy is unstable due to the major differences in atmospheric transmittance under various observation paths, a method for measuring radiation characteristics of an aircraft engine's hot parts and skin using a cooled middle-wave infrared camera is proposed. Based on the analysis of the aircraft's infrared radiation characteristics, the atmospheric transmission model of any observation path was revised, the absolute radiation correction model was established, and the temperature inversion equation was calculated. Then, we used the quasi-Newton method to calculate the skin temperature and discussed uncertainty sources. After the theoretical study, an outfield test was carried out. A middle-wave infrared camera with a wavelength of 3.7–4.8 μm was applied to the actual experimental observation of the turbofan civil aviation aircraft. The ground observation distance was 15 km, and the flying height was 3 km. When implementing temperature inversion with the method presented in this paper, the surface temperature of the aircraft engine hot parts was 381 K, the correction uncertainty was ± 10 K, the surface temperature of the skin was 296 K, and the correction uncertainty was ± 6 K. As the experiment showed, the method in this paper can effectively implement infrared target temperature inversion and provide a reference for the quantification of infrared data.



Citation: Deng, X.; Wang, Y.; Han, G.; Xue, T. Research on a Measurement Method for Middle-Infrared Radiation Characteristics of Aircraft. *Machines* **2022**, *10*, 44. <https://doi.org/10.3390/machines10010044>

Academic Editor: Feng Gao

Received: 1 December 2021

Accepted: 4 January 2022

Published: 7 January 2022

Publisher's Note: MDPI stays neutral with regard to jurisdictional claims in published maps and institutional affiliations.



Copyright: © 2022 by the authors. Licensee MDPI, Basel, Switzerland. This article is an open access article distributed under the terms and conditions of the Creative Commons Attribution (CC BY) license (<https://creativecommons.org/licenses/by/4.0/>).

Keywords: atmospheric transport model; uncertainty analysis; middle infrared; quasi-Newton method; temperature inversion

1. Introduction

The infrared radiation characteristics of highly maneuverable targets and their information interpretation are an important basis for target detection, recognition, and tracking [1]. The technical tackling of stealth materials on the surface of aircraft and the precise strike of suspicious targets in the air are in a great need of the real radiation characteristics of aircraft targets [2,3]. Therefore, measuring the infrared radiation characteristics of aircraft targets is not only conducive to infrared early warning and night reconnaissance of enemy flying targets, but also serves as an important reference value for improving the maneuverability and concealment of one's own aircraft [4]. Infrared radiation data contain a large number of target characteristics, electromagnetic characteristics, and background information. With the explosive demand for infrared technology and infrared systems in the aviation field, many experts have increasingly conducted in-depth research on the infrared radiation characteristics of targets, showing a trend of blooming flowers. The past decades have seen the rapid development of target infrared radiation characteristic measurement in many methods. Based on the principles of thermodynamics and aerodynamics, the radiation intensity characteristic model of the aircraft skin, tail nozzle, and plume was established [5–7]. The authors of [8] made important contributions to the construction of the ground-to-space radiometric model of space targets. In the absence of external field test conditions, infrared target simulation data are widely used in the simulation measurement of aircraft radiation characteristics [9–12]. Taking into account the actual influencing factors,

the real-time calibration and correction target infrared radiation measurement methods are proposed [13,14]. However, there are generally few measurements of aircraft radiation characteristics under high-speed navigation, and most experiments ignore the problem of atmospheric correction on the observation path in actual measurements.

In this paper, we set up a refrigerated middle-wave infrared camera to observe turbofan civil aircraft under high-speed navigation. A refrigerated area array middle-wave infrared camera is set up on the ground, for which the lens can be adjusted in elevation and azimuth directions. As the observation target of a civil aircraft in the air navigation state, the observation distance of the two can be calculated by using the horizontal and vertical distances between the imaging camera and the aircraft. By learning the infrared radiation source of aircraft targets and considering the difference in atmospheric transmittance at different observation angles from ground to air, the atmospheric transmission model of any observation path is revised. Based on the establishment of the absolute radiation calibration model, the inversion formula for the surface temperature of the fuselage is calculated; then, the factors that may induce temperature errors in the actual measurement process are discussed. In addition, on the basis of theoretical analysis, a radiation measurement experiment is carried out on a civil aviation aircraft in a flight state, collecting the measured radiation characteristic data of the flying target, inverting the target temperature, and calculating the temperature measurement error.

2. Infrared Radiation Characteristics of Aircraft

As shown in Figure 1, the infrared radiation sources of an aircraft flying in the atmosphere include the skin radiation heated by the engine's hot parts, the thermal radiation of the tail flame high-temperature gas, the skin radiation of the fuselage, the reflection of the ground radiation and the reflection of sky radiation. Among them, the reflection of sky radiation is mainly composed of the reflection of solar radiation and the reflection of atmospheric background radiation [15].

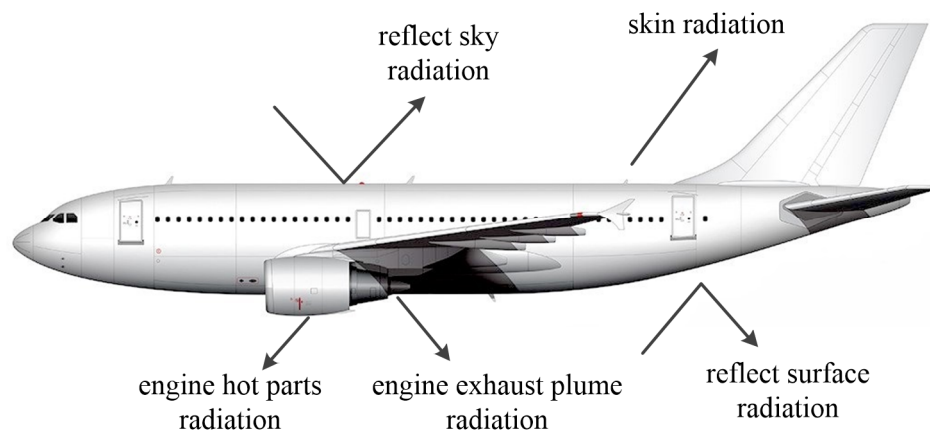


Figure 1. Distribution of infrared radiation sources of civil aircraft flying at high speed in the air.

The high-altitude aircraft target can be regarded as flying parallel to the ground; along the side observation direction of the infrared camera, the high-temperature gas at the tail of the aircraft is blocked to a certain extent. Thus, for the various thermal radiations of the aircraft itself, the skin radiation of the engine hot parts and the skin radiation of the aircraft fuselage will be focused on in the observation. The ground radiation is mostly dominated by long-wave radiation, and the solid angle of the ground radiation received by the side of the aircraft is small so that the skin radiation of the aircraft itself is much larger than the ground object radiation reflected by the aircraft [16]. The atmospheric radiation reflected by the aircraft has a low emissivity and a small amount of radiation, which is lower than that of the aircraft skin itself [17]. In short, the skin radiation can be approximated as the skin's own thermal radiation.

Any object whose temperature is not equal to absolute zero is a heat source that spontaneously emits infrared radiation. When the temperature is T , the spectral radiance of blackbody radiation is given by the blackbody radiation law [18].

$$M(\lambda) = \frac{c_1}{\lambda^5} \cdot \frac{1}{e^{(c_2/\lambda T)} - 1} \quad (1)$$

where c_1 denotes the first radiation constant, c_2 denotes the second radiation constant, λ denotes the wavelength, and T denotes the thermodynamic temperature.

The aircraft skin is regarded as both a Lambert reflector with uniform radiance in all directions and a gray body. According to the Lambertian radiation relationship, the radiance of the aircraft skin is:

$$L = \frac{\varepsilon}{\pi} \int_{\lambda_1}^{\lambda_2} M(\lambda) d\lambda = \frac{\varepsilon}{\pi} \int_{\lambda_1}^{\lambda_2} \frac{c_1}{\lambda^5} \frac{1}{e^{(c_2/\lambda T)} - 1} d\lambda \quad (2)$$

where ε denotes the aircraft surface emissivity, λ_1 denotes the starting wavelength of the camera, and λ_2 denotes the ending wavelength of the camera.

2.1. Aircraft Skin Infrared Radiation

An aircraft flying at high speed in the atmosphere will rub against the gas flowing over the surface of the fuselage in the air, generating a large amount of thermal energy to increase the temperature of the aircraft skin and emit a quantity of infrared radiation. The temperature of the aircraft skin has a connection to the flight parameters, aerodynamic shape, and atmospheric conditions of the aircraft. The aircraft skin temperature is approximated by the stagnation temperature of the static point on the aircraft skin surface [19], which can be expressed as:

$$T_r = T_0 \cdot \left(1 + r \cdot \frac{\gamma - 1}{2} \cdot Ma^2\right) \quad (3)$$

where T_0 denotes the thermodynamic temperature of the atmosphere around the aircraft skin; r denotes the temperature recovery coefficient, generally taken as 0.82; γ denotes the ratio of the air constant pressure heat capacity to the constant volume heat capacity, usually 1.3; and Ma denotes the Mach number of the aircraft.

2.2. Engine Hot Parts' Infrared Radiation

Figure 2 demonstrates a schematic diagram of the general structure of the turbofan engine ordinarily used in civil aviation aircraft. The fan is located at the forefront, followed by the part surrounding the turbine shaft and wrapped in the bypass air duct. From front to back, they are the high-pressure compressor, the combustion chamber, the high-pressure turbine, the low-pressure turbine, and finally, connection to the exhaust nozzle [20].

As the three important components at the core of turbofan engines, the high-pressure compressor, combustion chamber, and high-pressure turbine provide the main heat radiation for the entire engine and are the predominant positions for observing the engine's hot parts. The test conducted by engineer Yumei Wang of the Chinese Flight Test Establishment on the wall temperature of the engine's hot parts can roughly determine that when the ground temperature is 34–35 °C and the engine is in the state of low non-afterburning on the ground, the wall temperature of aircraft's hot parts is about 70–100 °C, can reach a maximum of 170 °C in the state of a large afterburner, and can reach 190 °C in the state of a large afterburner in the air [21]. Since the core of the aircraft engine is wrapped in an outer duct full of cold air, and the aircraft skin is constantly exchanging heat with the high-altitude cold air during the high-speed flight, the aircraft skin temperature of the hot parts of the engine is much lower than the working temperature of the inner core machine [22].

This means that the aircraft skin's infrared radiation of the engine hot parts in the air flight is affected by the heat transfer of the high-temperature core engine and the external airflow.

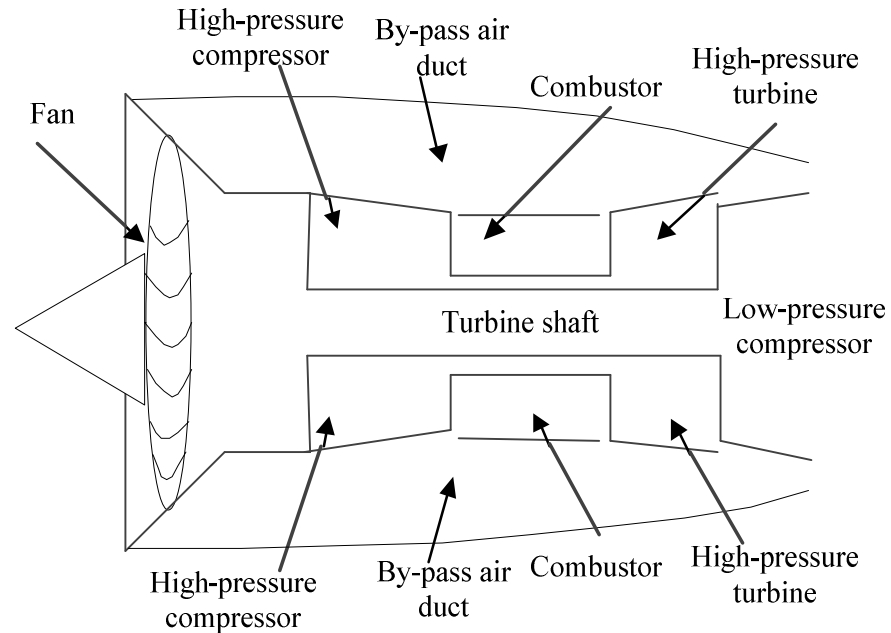


Figure 2. Schematic diagram of turbofan engine structure.

2.3. Reflected Solar Radiation

Solar radiation is consistent with the absolute blackbody radiation of 5900 K, and its radiation energy is projected onto the Earth's surface after being absorbed by the atmosphere by about 35%. The solar radiation reflected by the aircraft skin also belongs to graybody radiation [23], which can be expressed as:

$$L_{sun} = \frac{E}{\pi} \cdot (1 - 0.35) \cdot (1 - \varepsilon) \cdot \eta_{\lambda_2 - \lambda_1} \quad (4)$$

$$\eta_{\lambda_1 - \lambda_2} = \frac{\int_{\lambda_1}^{\lambda_2} M(\lambda) d\lambda}{\int_0^{\infty} M(\lambda) d\lambda} \quad (5)$$

where E denotes the effective radiant illuminance of the sun, and ε denotes the surface emissivity of the aircraft. If the aircraft is sailing at night, it will not be considered. If the aircraft is working at night, L_{sun} is not considered.

3. Atmospheric Transmission Model

During the propagation of infrared radiation in the atmosphere, radiation is absorbed and scattered by gas molecules and aerosol particles in the atmosphere, which leads to the attenuation of infrared radiation energy [24]. The relationship between the attenuation coefficient and transmittance in the atmosphere is:

$$\tau(\lambda) = \exp(-\mu(\lambda) \cdot x) \quad (6)$$

where x denotes the length of the transmission path, $\tau(\lambda)$ denotes the atmospheric transmittance, and $\mu(\lambda)$ denotes the attenuation coefficient.

As the uniformity of the atmosphere in the horizontal direction is greater than that in the vertical direction [25], to conveniently calculate the attenuation of infrared radiation from the atmosphere, the atmosphere between the aircraft target and the ground is divided vertically into multiple layers with a height of Δh , as given in Figure 3. The aircraft's

flying height is H , and the ground distance is L . The total transmission path length in the line-of-sight direction can be obtained by the transmission path length of each layer.

$$x = \sum_{i=1}^n x_i = n \cdot \Delta x \tag{7}$$

where x denotes the total transmission path length; Δx denotes the transmission path length of each layer; n denotes the total number of divided layers; i denotes the number of layers, where the first layer is closest to the ground; and x_i denotes the transmission path length of layer i .

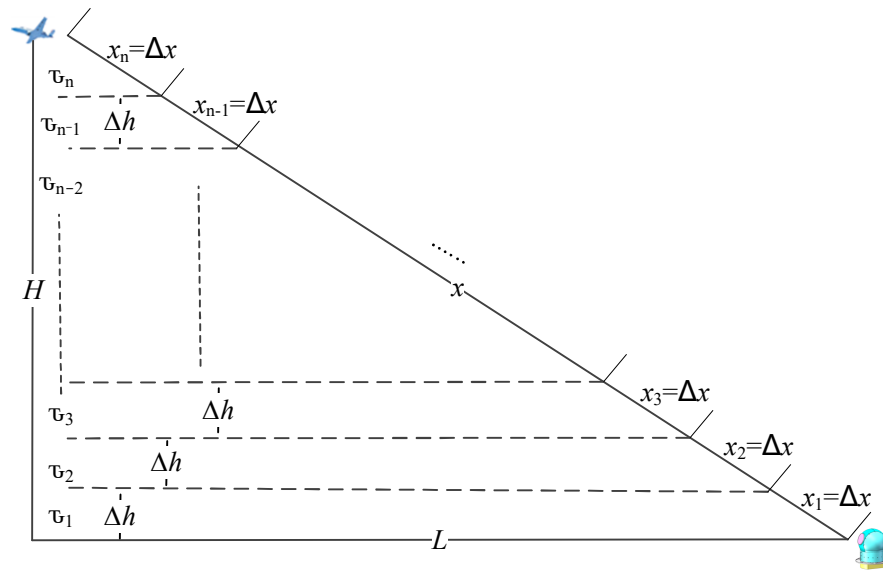


Figure 3. Schematic diagram of turbofan engine structure.

The atmospheric temperature and pressure in each layer are uniform and constant, and the molecules are in a state of local thermal equilibrium. Furthermore, the total atmospheric transmittance is the product of the atmospheric transmittance of each layer.

$$\tau(\lambda) = \prod_{i=1}^n \tau_i(\lambda) \tag{8}$$

where $\tau(\lambda)$ denotes the total atmospheric transmittance, and $\tau_i(\lambda)$ denotes the atmospheric transmittance of layer i .

3.1. Absorption of H₂O Molecules

The ozone in the atmosphere is mainly concentrated at an altitude of 20–50 km, and the content of methane is low. Therefore, water vapor and carbon dioxide are dominant in the absorption of infrared radiation in the troposphere [26]. Generally, the amount of water vapor in the atmosphere is expressed by the amount of precipitation. As shown in Figure 4, assuming that the atmosphere is a cylinder with a bottom surface ΔS equal to the camera aperture and a length x equal to the transmission distance, the height w at which water vapor condenses into liquid water in the cylinder is called precipitable water vapor [27].

$$w = H_r(h) \cdot H_a(T) \cdot x \tag{9}$$

where w denotes the amount of precipitable water vapor, $H_r(h)$ denotes the relative humidity at altitude h , $H_a(T)$ denotes the saturated water vapor content related to the temperature T , and x denotes the infrared radiation transmission distance.

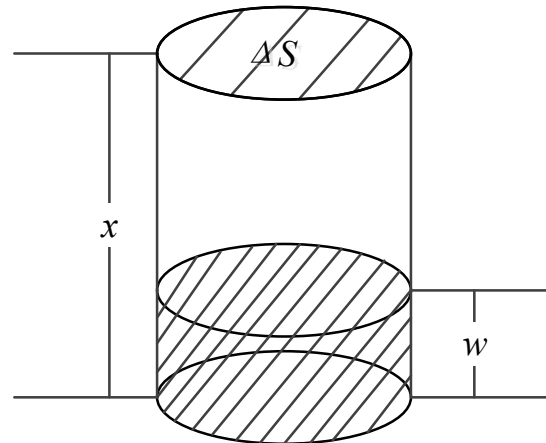


Figure 4. Precipitable water vapor (PWV).

We can fit the data between the amount of precipitable water vapor at sea level and the average atmospheric transmittance between 3.7 and 4.8 μm with Equation (10) [27].

$$\tau_{\text{H}_2\text{O}}(\lambda) = Kw^B + 1 \quad (10)$$

where $\tau_{\text{H}_2\text{O}}(\lambda)$ denotes the atmospheric transmittance of H_2O , K denotes the multiple factor, and B denotes the index coefficient.

At the same time, the root mean square error (RMSE) is used as the standard for evaluating the fitting accuracy. The closer the fitted curve fits the real original data points, the smaller the RMSE, and the higher the fitting accuracy. The fitting coefficients are presented in Table 1.

$$RMSE = \sqrt{\frac{\sum_{r=1}^R (\tau_r - \tau'_r)^2}{R}} \quad (11)$$

where R denotes the total number of samples, r denotes the number of sample sequences, τ_r denotes the original value, and τ'_r denotes the fitted value.

Table 1. Fitting coefficient of PWV and atmospheric transmittance.

$\lambda/\mu\text{m}$	K	B	RMSE
3.7	−0.009342	0.9394	0.0001799
3.8	−0.005108	0.9747	0.0003843
3.9	−0.002059	0.9672	0.0002266
4.0	−0.001522	1.046	0.0002771
4.1	−0.001672	1.033	0.0002825
4.2	−0.001967	1.008	0.0001799
4.3	−0.003412	1.024	0.0003843
4.4	−0.006245	0.9621	0.0004364
4.5	−0.01069	0.8924	0.0006834
4.6	−0.03198	0.7301	0.002214
4.7	−0.05147	0.6721	0.002514
4.8	−0.1096	0.5430	0.003284

The atmospheric transmittance of H_2O in the line-of-sight observation direction needs to be corrected by the correction factor β_1 before it can be used.

$$\tau_{\text{H}_2\text{O}}(\lambda) = K(\lambda) \cdot [H_r(h) \cdot H_a(T) \cdot x \cdot \beta_1]^{B(\lambda)} + 1 \quad (12)$$

$$\beta_1 = \left(\frac{P}{P_0}\right)^{0.5} \left(\frac{T_0}{T}\right)^{0.25} \quad (13)$$

where β_1 denotes the correction factor, P denotes the atmospheric pressure at altitude h , P_0 denotes the atmospheric pressure at sea level, T denotes the temperature at altitude h , T_0 denotes the temperature at sea level, and x denotes the infrared radiation transmission distance.

The atmospheric transmittance of H_2O in the line-of-sight observation direction needs to be corrected by the correction factor β_1 before it can be used.

3.2. Absorption of CO_2 Molecules

Similar to H_2O , we use Equation (14) to fit the CO_2 transmittance data at different distances from sea level in each band [28]. Table 2 illustrates the fitting coefficients.

$$\tau_{CO_2}(\lambda) = A \cdot x^D + 1 \tag{14}$$

where $\tau_{CO_2}(\lambda)$ denotes the atmospheric transmittance of CO_2 , A denotes the multiple factor, D denotes the index coefficient, and x denotes the infrared radiation transmission distance.

Table 2. Fitting coefficient of CO_2 and atmospheric transmittance.

$\lambda/\mu\text{m}$	A	D	$RMSE$
3.7	−0.0001819	0.5540	0.0002727
3.8	−0.0004674	0.6484	0.0005531
3.9	−0.0002748	1.254	0.0001910
4.0	−0.002860	1.035	0.0002863
4.1	−0.2080	0.3545	0.005455
4.2	−0.9906	0.0080	0.01117
4.3	−0.9786	0.0637	0.02359
4.4	−0.5363	0.2544	0.05889
4.5	−0.005162	0.9883	0.0004551
4.6	−0.001919	0.9714	0.0002216
4.7	−0.009497	0.9446	0.001027
4.8	−0.009232	0.5967	0.003324

The correction factor β_2 is utilized to correct the data that are only applicable to sea level to obtain the atmospheric transmittance of CO_2 under any observation path.

$$\tau_{CO_2}(\lambda) = A(\lambda) \cdot (x \cdot \beta_2)^{D(\lambda)} + 1 = A(\lambda) \cdot \left[x \cdot \left(\frac{P}{P_0} \right)^{0.5} \frac{T_0}{T} \right]^{D(\lambda)} + 1 \tag{15}$$

where P denotes the atmospheric pressure at altitude h , P_0 denotes the atmospheric pressure at sea level, T denotes the temperature at altitude h , T_0 denotes the temperature at sea level, and β_2 denotes the correction factor.

3.3. Scattering of Aerosols and Particles

Suspended particles, aerosols, etc., contained in the atmosphere will change the original transmission direction of infrared radiation, resulting in scattering attenuation, including Rayleigh scattering and Mie scattering. For atmospheric transmittance caused by scattering, the meteorological range is generally used as the reference [29].

$$\tau_{SC0}(\lambda) = \exp\left[-\frac{3.912}{V} \cdot \left(\frac{0.55}{\lambda}\right)^q \cdot x\right] \tag{16}$$

where τ_{SC0} the scattering transmittance at sea level, V denotes the meteorological optical range, q denotes the correction factor, and there is the following relationship:

$$\begin{cases} q = 0.585 V^{1/3} (V < 6 \text{ km, poor visibility}), \\ q = 1.3 (V = 6\text{--}80 \text{ km, moderate visibility}), \\ q = 1.6 (V > 80 \text{ km, clear visibility}). \end{cases}$$

Taking into account the influence of altitude on aerosol and other particles, the scattering transmittance is corrected.

$$\tau_{SC}(h) = \tau_{SC0} \exp(-h/h_\delta) \tag{17}$$

where h_δ denotes the feature height, usually 1.2 km.

Therefore, the scattering transmittance of different heights can be described as:

$$\tau_{SC}(\lambda) = \left\{ \exp\left[-\frac{3.912}{V} \cdot \left(\frac{0.55}{\lambda}\right)^q \cdot x\right] \right\}^{\exp(-h/1.2)} \tag{18}$$

To summarize, the total atmospheric transmittance of each band can be obtained as:

$$\tau(\lambda) = \tau_{H_2O}(\lambda) \cdot \tau_{CO_2}(\lambda) \cdot \tau_{SC}(\lambda) \tag{19}$$

4. Theoretical Model of Temperature Measurement

4.1. Background Radiation

Figure 5 demonstrates the process of the infrared camera receiving radiation signals. While aerial targets are imaged on the middle-wave infrared camera through the atmosphere, the background radiation of non-targets is also imaged on the infrared camera. The radiance of the non-target background pixel L_{BP} in the infrared image consists of the atmospheric background radiation L_B after atmospheric attenuation and the thermal detector radiation L_E . The radiance of the target pixel L_{TP} in the infrared image is composed of the target actual radiation L_T through the atmosphere and the background pixel radiation L_{BP} .

$$L_{BP} = \tau(\lambda) \cdot L_B + L_E \tag{20}$$

$$L_{TP} = \tau(\lambda) \cdot (L_T + L_B) + L_E \tag{21}$$

where L_{BP} denotes the background pixel radiation received by the infrared camera, L_B denotes the atmospheric background radiation, $\tau(\lambda)$ denotes the atmospheric transmittance, L_E denotes the thermal radiation of the detector itself, L_{TP} denotes the target pixel radiance received by the infrared camera, and L_T denotes the actual radiation of target.

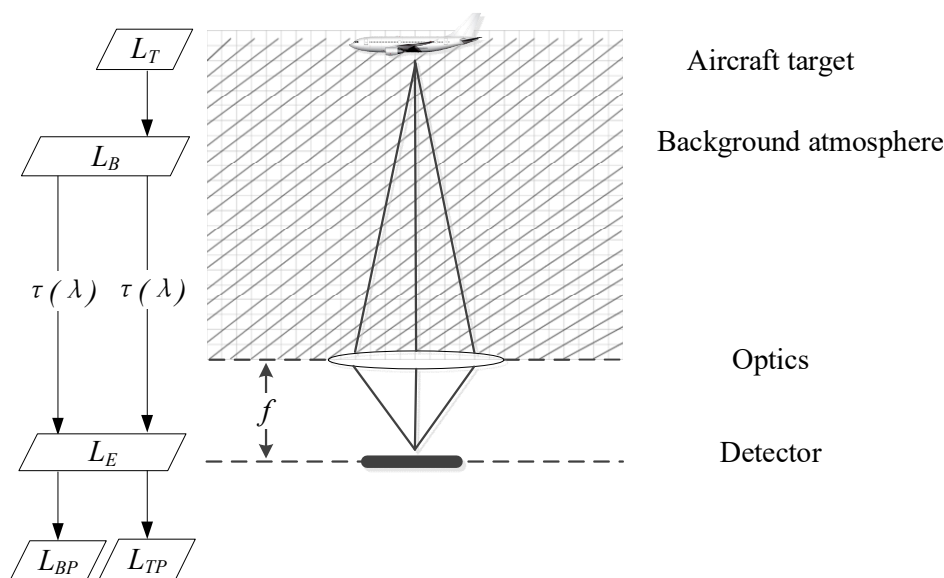


Figure 5. Process of camera receiving infrared radiation.

Therefore, the radiance of the target signal L_{DT} received by the camera at the entrance pupil can be obtained by subtracting the entrance pupil radiance of the target pixel and the entrance pupil radiance of the background pixel.

$$L_{DT} = L_{TP} - L_{BP} = \tau(\lambda) \cdot L_T \quad (22)$$

4.2. Absolute Radiometric Calibration Model

There is a corresponding relationship between the radiation response collected by the detector and the intensity of the radiation source [30]. The purpose of absolute radiometric calibration is to obtain the linear relationship between the digital number of the radiometric response and the radiance of the entrance pupil.

$$G = m \cdot L + n \quad (23)$$

where G is the radiation response value collected by the middle-wave camera, m denotes the detector responsivity, n denotes the fixed offset of the infrared detector at a dark level, and L_G denotes the radiance at the optical entrance pupil of the detection system.

By collecting two sets of (G, L) values at different blackbody temperatures, the coefficient (m, n) in Equation (23) can be calculated to obtain the relationship between the radiation response and the entrance pupil radiance. During the blackbody calibration process, the camera lens is placed close to the blackbody to reduce the attenuation. It is considered that the radiance at the optical entrance pupil is equivalent to the radiance of the blackbody, and the radiance of the blackbody can be calculated by Equation (2) using the blackbody temperature and the blackbody emissivity.

4.3. Temperature Inversion Model

The radiation response value of the target signal received at the entrance pupil of the mid-wave infrared camera can be obtained by subtracting the radiation response of the background pixel from the collected radiation response of the target pixel. Therefore, the collected target signal radiation response value can be represented as:

$$G_{DT} = G_{TP} - G_{BP} = (m \cdot L_{TP} + n) - (m \cdot L_{BP} + n) = m \cdot L_{DT} \quad (24)$$

It can be seen from Equation (2) that when the system parameters and atmospheric transmittance are known, the radiance of the target signal reaching the entrance pupil is only related to the target's own temperature T . Then the variable $I(T)$, which is only related to T , is used to represent the radiance of the target signal reaching the entrance pupil.

$$I(T) = \tau(\lambda) \cdot L_T = \frac{\varepsilon}{\pi} \int_{\lambda_1}^{\lambda_2} \tau(\lambda) \cdot \frac{c_1}{\lambda^5} \cdot \frac{1}{e^{(c_2/\lambda T)} - 1} d\lambda \quad (25)$$

In an ideal state, the radiance of the target signal arriving at the entrance pupil should be equal to the radiance of the entrance pupil received by the camera. Therefore, the objective function $f(T)$ is established.

$$f(T) = (L_{DT} - I(T))^2 = \left(\frac{G_{DT}}{m} - I(T)\right)^2 \quad (26)$$

We can solve the optimal parameter T to minimize the objective function.

$$\operatorname{argmin}_T f(T) = \operatorname{argmin}_T \left(\frac{G_{DT}}{m} - I(T)\right)^2 \quad (27)$$

There must be a maximum value of T_{MAX} for the skin temperature of the aircraft in the air flight state, which is roughly estimated to be 443 K in [22], and the temperature must be higher than the atmospheric temperature T_H at the flight altitude H . Therefore, $M(\lambda, T)$ is continuous in the closed interval $3.7 \mu\text{m} \leq \lambda \leq 4.8 \mu\text{m}$ and $T_H \leq T \leq T_{MAX}$, so $I(T)$ is

continuous on the closed interval of λ and T . We can take the partial derivative of $M(\lambda, T)$ with respect to T :

$$M'_T(\lambda, T) = -\frac{c_2}{\lambda} \cdot M^2(\lambda, T) \cdot \exp\left(\frac{c_2}{\lambda T}\right) \cdot T^{-2} \tag{28}$$

Each factor of $M'_T(\lambda, T)$ is continuous in the closed interval of λ and T . It can be deduced that the product of each continuous factor is also continuous in the closed interval of λ and T . Similarly, $M(\lambda, T)$ and $M'_T(\lambda, T)$ are continuous in the closed interval of λ and T , so $I(T)$ has a continuous derivative $I'(T)$ in the closed interval of T .

$$I'(T) = \frac{\varepsilon}{\pi} \int_{\lambda_1}^{\lambda_2} M'_T(\lambda, T) d\lambda \tag{29}$$

Therefore, the partial derivative of the objective function with respect to T exists.

$$\nabla f(T) = 2 \cdot (L_{DT} - I(T)) \cdot I'(T) \tag{30}$$

Similarly, $\nabla^2 f(T)$ also exists as the second partial derivative of the objective function $f(T)$ with respect to T .

In this paper, the quasi-Newton method is used to iterate to find the local minimum of the objective function through a given initial value. This process is illuminated in Figure 6. To realize the optimization of the one-dimensional unconstrained objective function, it is approximated by the second-order Taylor expansion, and the extreme point is obtained.

$$T_{j+1} = T_j - \frac{\nabla f(T_j)}{\nabla^2 f(T_j)} \tag{31}$$

where j denotes the number of iterations, T_j denotes the temperature of the j th iteration, $\nabla f(T)$ denotes the partial derivative of the objective function, and $\nabla^2 f(T)$ denotes the second partial derivative of the objective function.

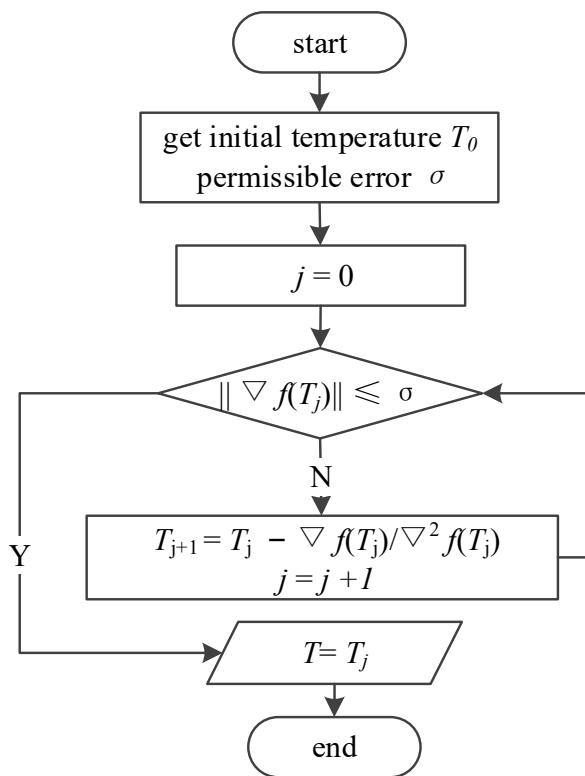


Figure 6. Flow chart of quasi-Newton method.

Equation (31) is used as an iterative formula. According to the given initial temperature T_0 and allowable error σ , by measuring the gradient value change, if the absolute value is less than the allowable error, the point is considered the extreme point, and the iteration output result is ended. Otherwise, the iteration is continued.

5. Radiation Characteristic Measurement and Analysis

5.1. Experimental Conditions

The observation site is the rooftop on the eighth floor of Building One, the Shanghai Institute of Technical Physics, the Chinese Academy of Sciences, Shanghai. The longitude of the geographical coordinates is 121.4917, and the latitude is 31.2859. The test time was 21:00 on June 5, 2021, the meteorological sight distance of that day was 12 km, and the ground temperature was 27 °C, which is 300 K. The observation target was MU8427 flying from Baotou Donghe Airport to Shanghai Pudong Airport. The aircraft type was BOEING737-800, the fuselage was 39.5 m, the flying height was 3 km, the ground distance was 15 km, and the flying speed was 588 km/h, which is 0.47 Ma. The observation site mainly observes aircraft flying at night, so the influence of solar radiation L_{sun} was not considered. According to the information, this material on the surface of the civil aviation aircraft skin was mainly a coating of aluminum powder and phenolic resin [31], so the emissivity $\varepsilon = 0.9$.

5.2. Temperature Inversion

After the analysis of the above characteristics, the main steps of temperature inversion included:

- We first calculated the atmospheric transmittance $\tau(\lambda)$ of each band and substituted it into the objective function $f(T)$;
- Second, we calculated the entrance pupil radiance L_{DT} of the target signal by the absolute radiometric calibration model;
- Third, the quasi-Newton method was used to find the optimal solution T of the objective function $f(T)$.

We stratified the atmosphere with a height of 3 km and took the height of a single layer $\Delta h = 0.1$ km; then, the length of the single-layer observation path was $\Delta x = 0.5099$ km, which was divided into 29 layers. According to the hourly data of ERA5 released by the European Centre for Medium-Range Weather Forecasts, the detailed meteorological data at the time of camera imaging were acquired. The atmospheric parameters of each layer are detailed in Table 3.

Table 3. Atmospheric parameters of each layer.

Number of Layer	Atmospheric Pressure/hpa	Temperature/K	Relative Humidity/%	Saturated Water Vapor Content/g·(cm ³) ⁻¹
29	685.2222	278.1854	29.7408	7.0809
28	696.3333	279.1531	30.5621	7.5911
27	707.4444	280.2053	30.7385	8.2073
26	718.5556	281.3268	30.3619	8.7861
25	729.6667	282.4782	29.6096	9.4842
24	740.7778	283.6197	28.6605	10.2182
23	751.8889	284.7116	27.6929	11.0661
22	763.0000	285.7376	26.7791	11.8898
21	774.1111	286.7389	25.7333	12.6950
20	785.2222	287.7575	24.3524	13.4914
19	796.3333	288.7984	22.5393	14.4903
18	807.4444	289.8520	20.2653	15.5576
17	818.5556	290.8794	17.8935	16.5653
16	829.6667	291.8237	16.0223	17.7032
15	840.7778	292.6548	14.7151	18.5310

Table 3. Cont.

Number of Layer	Atmospheric Pressure/hpa	Temperature/K	Relative Humidity/%	Saturated Water Vapor Content/g·(cm ³) ⁻¹
14	851.8889	293.3754	13.3739	19.3996
13	863.0000	293.975	12.2206	20.2660
12	874.1111	294.4066	13.5674	20.8110
11	885.2222	294.6472	19.2452	21.0906
10	896.3333	294.8249	27.0594	21.2951
9	907.4444	295.1062	33.7232	21.6279
8	918.5556	295.5460	38.0968	22.2015
7	929.6667	296.1275	40.4114	23.1203
6	940.7778	296.8157	40.8428	24.2205
6	951.8889	297.5547	39.4749	24.6124
5	963.0000	298.1789	37.5592	25.3487
4	974.1111	298.260	39.1968	25.5416
3	985.2222	299.3304	48.9127	28.2848
2	996.3333	299.9225	71.2322	29.1840
1	1007.444	300.0181	88.5324	29.3277

We can substitute the parameters of Table 3 into Equations (12), (15), (18) and (19) to obtain the atmospheric transmittance of each band (see Table 4 for details).

Table 4. Atmospheric transmittance of each band.

$\lambda/\mu\text{m}$	$\tau(\lambda)$	$\lambda/\mu\text{m}$	$\tau(\lambda)$
3.7	0.7929	4.3	1.8464×10^{-3}
3.8	0.8235	4.4	2.5026×10^{-7}
3.9	0.8515	4.5	0.1697
4.0	0.8359	4.6	0.6249
4.1	0.7080	4.7	0.4523
4.2	0.1334	4.8	0.3880

We can perform an absolute radiation correction experiment 15 min before the imaging experiment to minimize the error caused by the excessive difference from the observation experiment environment. In the experiment, a surface source blackbody with a temperature range of 0–100 °C (273–373 K), a temperature accuracy of ± 0.02 , and an emissivity of 0.99 produced by Electro Optical Industries was selected. The blackbody temperature starts at 273 K and ends at 308 K in steps of 5 K, with a total of eight calibration points. The medium wave camera collects 100 frames of radiation response data for each calibration point and obtains the average value. At the same time, the blackbody radiance at the corresponding temperature of each calibration point is calculated.

The coefficient of the linear relationship in Equation (23) is obtained by fitting the radiation response data of the detector at each calibration point and the blackbody's entrance pupil radiance.

$$G = 4.702 \times 10^7 \times L_{DN} + 5005 \quad (32)$$

The calibration result is displayed in Figure 7. It can be seen that the relationship between the two has good linearity and can be used for linear calibration.

The image obtained by the middle-wave infrared camera on the civil aviation aircraft in the test is shown in Figure 8. The side profile of the aircraft is obvious. The pixels near the high hot spots in the middle of the aircraft side are selected as the signal pixels of the engine thermal components, and the pixels near the head, tail, and top of the aircraft are selected as the signal pixels of the hot parts of the engine.

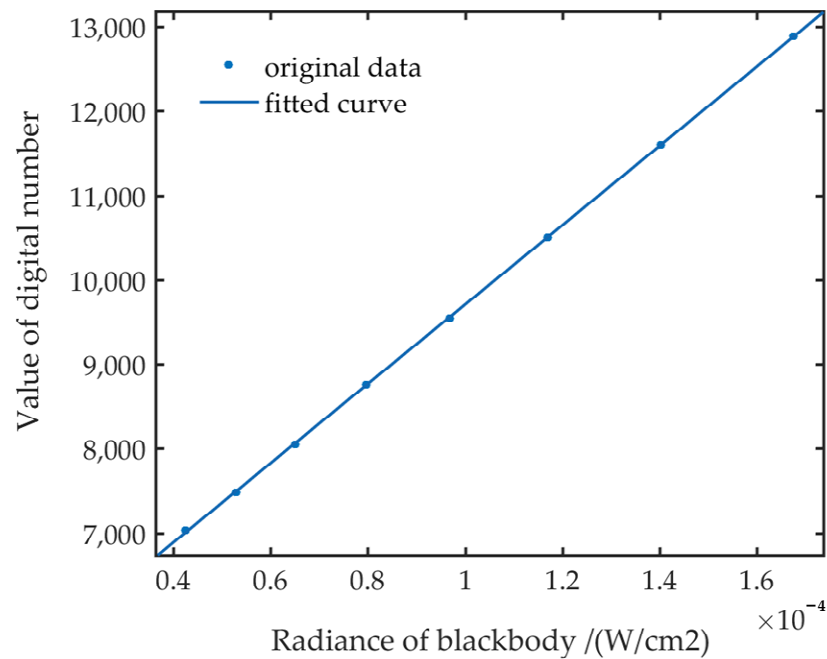


Figure 7. Corresponding relationship between digital response value and blackbody radiance at different temperatures.

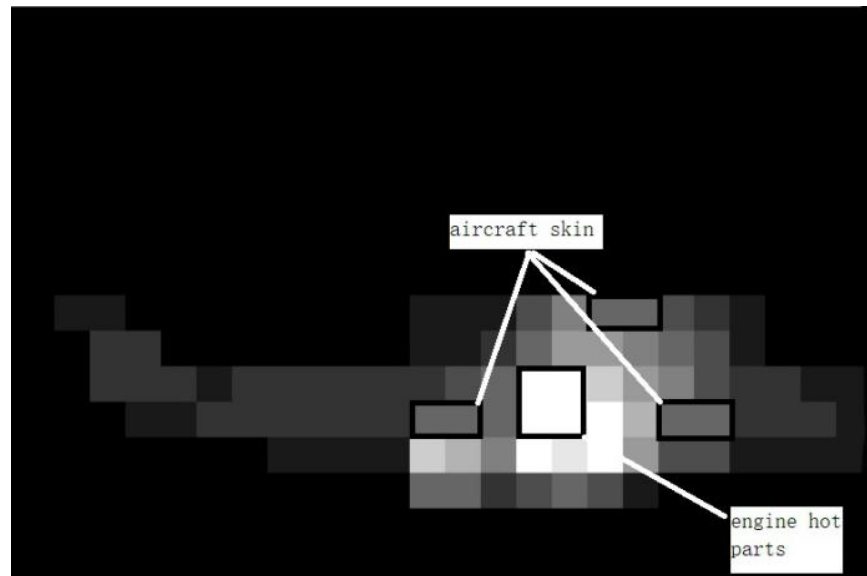


Figure 8. Middle-wave infrared image of civil aviation aircraft.

The radiation response digital number value of the target pixel $G_{TP-skin} = 11,385$, $G_{TP-hot} = 26,564$, and the digital number values of the background pixel $G_{BP} = 10,171$ are substituted into Equations (22) and (32) to obtain the entrance pupil radiance of the target signal $L_{DT-skin} = 4.5512 \times 10^{-6} \text{W}/\text{cm}^2$, $L_{DT-hot} = 3.4864 \times 10^{-4} \text{W}/\text{cm}^2$. The stagnation point temperature of the skin is calculated by substituting the relevant atmospheric data into Equation (3), and it is set as the initial value of the skin temperature $T_{skin0} = 285.7439 \text{ K}$, and the wall temperature of the engine's hot parts under the ground non-afterburner state is set as the initial value $T_{hot0} = 343 \text{ K}$.

Then, we can use the quasi-Newton method to bring $L_{DT-skin}$ and L_{DT-hot} into the objective function for iterative calculations to solve the optimal solutions T_{skin} and T_{hot} , respectively. As the values of $L_{DT-skin}$ and L_{DT-hot} are too small, to simplify the calculation

of the quasi-Newton method, $L_{DT-skin}$ and L_{DT-hot} are multiplied by 10^8 , respectively, and the $I(T)$ in the objective function is also multiplied by 10^8 .

Finally, the optimal solution is solved $T_{skin} = 295.7791$ K, $T_{hot} = 381.1792$ K.

5.3. Measurement Uncertainty Analysis

According to the uncertainty caused by different reasons, there are two types of evaluation methods: uncertainty Type A evaluation and uncertainty Type B evaluation [32].

Uncertainty Type A evaluation is used to evaluate the standard uncertainty by statistical analysis of the observation sequence, and it is characterized by the experimental standard deviation.

$$\sigma_A(y) = \sqrt{\frac{\sum_{i=1}^n (y_i - \bar{y}_i)^2}{n}} \quad (33)$$

where σ_A denotes uncertainty Type A, \bar{y}_i denotes the average of the i th observation result y_i , and n denotes the number of statistics.

Uncertainty Type B evaluation is used to estimate the uncertainty by experiment or other information [32], which contains subjective identification components.

$$\sigma_B = \frac{a}{k_p} \quad (34)$$

where σ_B denotes uncertainty Type B, a denotes the half-width of the uncertainty of identification, and k_p denotes the inclusion factor. Generally, the confidence probability is 95%, and the inclusion factor is 1.96.

Comparing the atmospheric transmittance calculated using the atmospheric transmission model in the article with the Modtran calculation result, a relative uncertainty of 5.64% is obtained. The atmospheric transmittance $\tau(\lambda)$ is calculated by using the atmospheric transmittance of the 12 bands calculated in Table 4, and the atmospheric transmittance of the other fine bands is calculated using a cubic spline function with a 1 μ m spectrum. The interval is obtained as input interpolation. Combining the cubic spline function, it can be found [33] that the Newton tangent method is used in each interval to find the point of the longest bow height, that is, the point with the largest error, so as to obtain a calculation error with a relative uncertainty of 2.84%. A comprehensive introduction of $\sigma_\tau/\tau = 8.48\%$ relative uncertainty was found for atmospheric transmittance.

Due to the year-round flight takeoff and landing, the surface of the aircraft has different oxidation levels due to the difference in material composition and service life, and its actual emissivity has a certain deviation from the emissivity obtained from the data query. It is known from [31] that the half-width of the uncertainty of the emissivity of the skin is 0.05. Generally, the uncertainty inclusion factor of 1.96 is taken, and the relative uncertainty is $\sigma_\varepsilon/\varepsilon = 2.83\%$, where σ_ε denotes the uncertainty of emissivity.

Solar radiation is consistent with the absolute blackbody radiation of 5900 K, which is a popular assumption. However, for wavelengths exceeding 3 μ m, the blackbody approximation is still applicable, but at longer wavelengths, the corresponding blackbody temperature will change [34,35]. For non-night imaging, to ensure that the influence of changes in these parameters can be fully considered when calculating the solar radiation reflected by the aircraft skin, we use the maximum approximate deviation of the solar radiation and the absolute radiation of the 5900 K blackbody to calculate the uncertainty. The relative uncertainty of the solar radiation reflected by the aircraft skin is $\sigma_{L_{sun}}/L_{sun} = 6.24\%$.

When the blackbody is calibrated with absolute radiation, the temperature stability and emissivity error of the blackbody itself will bring about an uncertainty of about 0.9% [36]. At the same time, under different external conditions, the stability of the infrared camera will also change due to environmental changes. The uncertainty of the available radiation calibration of 0.96% is obtained by performing multiple absolute radiation calibration experiments on the blackbody. The total relative uncertainty of the available radiation calibration is $\sigma_{L_{DT}}/L_{DT} = 1.09\%$.

We can combine the above uncertainties to calculate the temperature uncertainty σ_T [32].

$$\sigma_T = \sqrt{\left(\frac{dT}{d\tau}\right)^2 \cdot \sigma_\tau^2 + \left(\frac{dT}{d\varepsilon}\right)^2 \cdot \sigma_\varepsilon^2 + \left(\frac{dT}{dL_{DT}}\right)^2 \cdot \sigma_{L_{DT}}^2 + \left(\frac{dT}{dL_{sun}}\right)^2 \cdot \sigma_{L_{sun}}^2} \quad (35)$$

Equation (35) can be simplified [37].

$$\sigma_T = \frac{k\lambda T^2}{hc} \sqrt{\left(\frac{\sigma_\tau}{\tau}\right)^2 + \left(\frac{\sigma_\varepsilon}{\varepsilon}\right)^2 + \left(\frac{\sigma_{L_{DT}}}{L_{DT}}\right)^2 + \left(\frac{\sigma_{L_{sun}}}{L_{sun}}\right)^2} \quad (36)$$

where k denotes Boltzmann's constant, h denotes Planck's constant, and c denotes the speed of light.

We can substitute each parameter into the calculation to obtain the temperature uncertainty of the aircraft skin $\sigma_{T_skin} = 5.48$ K and the temperature uncertainty of the engine thermal component skin $\sigma_{T_hot} = 9.14$ K. Taking into account the accuracy of the actual measurement, the results are rounded to obtain the temperature of the engine's hot parts and skin, $296 \text{ K} \pm 6 \text{ K}$ and $381 \text{ K} \pm 10 \text{ K}$, respectively.

6. Conclusions

This paper proposes a method to measure the infrared radiation characteristics of aircraft for mid-wave infrared cameras. It is verified through experiments that the atmospheric path of the target observation visual range is layered, and the atmospheric transmittance is calculated in sections, which can effectively be based on the actual situation. Obtaining the atmospheric transmittance under any observation path is more practical than simply using simulated atmospheric data to calculate the atmospheric transmittance. Secondly, a civil aviation aircraft with a ground distance of 15 km and a flying height of 3 km was observed in the field. Using the temperature inversion model and uncertainty analysis method proposed in this paper, the surface temperature of the hot parts of the aircraft engine was 381 K, and the estimated uncertainty was ± 10 K; for the aircraft skin's surface, the temperature was 296 K, and the estimated uncertainty was ± 6 K.

Author Contributions: Conceptualization, Y.W.; Investigation, X.D.; Methodology, X.D.; Software, X.D.; Formal analysis, X.D.; Writing—original draft, X.D.; Supervision, Y.W.; Project administration G.H. and Y.W.; Visualization, G.H.; Resources, Y.W., G.H. and T.X.; Writing—review and editing, T.X. All authors have read and agreed to the published version of the manuscript.

Funding: This research received no external funding.

Conflicts of Interest: The authors declare no conflict of interest.

References

1. Kou, T.; Zhou, Z.; Liu, H.; Yang, Z. Correlation between infrared radiation characteristic signals and target maneuvering modes. *Acta Opt. Sin.* **2018**, *38*, 37–45.
2. Du, S.; Yang, J.; Zeng, K.; Gao, Y.; Chen, S. Discussion on the infrared stealthy technique of aircraft. *Electron. Warf.* **2010**, *133*, 41–45.
3. Wang, C. Detecting and tracking technology about IR stealth target. *Infrared Laser Eng.* **2006**, *35* (Suppl. S1), 127–132.
4. Li, W.; Yan, S.; Hu, L.; Wu, Y.; Wang, C.; Ouyang, Y. A review of false alarm suppression technology for infrared early warning satellite. *Infrared Technol.* **2020**, *42*, 115–120.
5. Mao, X.; Hu, H.; Huang, K.; Liang, X. Calculation method for airplane IR radiation and atmospheric transmittance. *J. Beijing Univ. Aeronaut. Astronaut.* **2009**, *35*, 1228.
6. Kang, L.Z.; Zhao, J.S.; Li, Z.H. The overview of the research work developments on infrared signature of aircraft. *Infrared Technol.* **2017**, *39*, 105–115.
7. Zong, J.; Zhang, J.; Liu, D. Infrared Radiation Characteristics of the Stealth Aircraft. *Acta Photonica Sin.* **2011**, *40*, 289–294. [[CrossRef](#)]
8. Liu, Y.; Liu, X. Research on technology of ground-based infrared radiation feature measurement for space target. *Acta Opt. Sin.* **2014**, *34*, 123–129.

9. Wang, X.; Gao, S.; Jin, L.; Li, Z.; Li, F. Multi-band Infrared Radiation Characterization and Simulation Analysis for Aerial Target. *Acta Photonica Sin.* **2020**, *49*, 511002. [[CrossRef](#)]
10. Han, Y.; Xuan, Y. Effect of atmospheric transmission on IR radiation of feature target and background. *J. Appl. Opt.* **2002**, *4*, 8–11.
11. Liu, J.; Gong, G.; Han, L.; Gao, D. Modeling and simulation of airplane infrared characteristic. *Infrared Laser Eng.* **2011**, *40*, 1209–1213.
12. Yang, C.; Cao, L.; Zhang, J. Measurement of infrared radiation for target airplane based on real-time atmospheric correction. *Opt. Precis. Eng.* **2014**, *22*, 1751–1759. [[CrossRef](#)]
13. Yang, C.; Zhang, J.; Cao, L. Infrared radiation measurement based on real-time correction. *J. Infrared Millim. Waves* **2011**, *30*, 284–288. [[CrossRef](#)]
14. Sun, Z.; Chang, S.; Zhu, W. Radiometric calibration method for large aperture infrared system with broad dynamic range. *Appl. Opt.* **2015**, *54*, 4659–4666. [[CrossRef](#)]
15. Huang, W.; Ji, H. Effect of reflected background radiation by skin on infrared signature of subsonic aircraft (I): Methodology. *Infrared Laser Eng.* **2015**, *44*, 1699–1703.
16. Huang, W.; Ji, H. Effect of reflected background radiation by skin on infrared signature of subsonic aircraft (II): Application. *Infrared Laser Eng.* **2015**, *44*, 2039–2043.
17. Li, J.; Tong, Z.; Wang, C.; Chai, D.; Zhang, Z.B. IR radiation characteristics analysis and vulnerability assessment of aircraft. *Laser Infrared* **2013**, *43*, 180–185.
18. Chen, B.; Fang, Y.; Xu, X. Study on the IR radiation of aeroplane. *Aero Weapon.* **2005**, *4*, 30–32.
19. Wang, C.; Tong, Z.; Lu, Y.; Chai, D. Study on airplane's infrared radiation characteristics. *Laser Infrared* **2011**, *41*, 996–1001.
20. Chen, G. The development of civil high-bypass turbofans. *J. Aerosp. Power* **2019**, *3*, 56–61.
21. Xia, J.; Yang, Q.; Wang, H.; Wu, Y. Development analysis to after burner combustion technology of turbofan. *J. Aerosp. Power* **2020**, *4*, 17–21.
22. Wang, Y.; Chen, Z.L. Analysis of temperature field in nacelle for a turbofan engine. *Eng. Test* **2015**, *55*, 35.
23. Zhang, Z.; Tong, Z.; Wang, C.; Li, J. Modeling and simulation of airplane infrared characteristic along the sight line. *Laser Infrared* **2013**, *43*, 890–895.
24. Wu, H. Research in to theoretical calculation method on engineering of transmittance of infrared radiation through atmosphere. *Opt. Precis. Eng.* **1998**, *6*, 120–125.
25. Kang, D.; Cheng, B.; Gao, J. Different algorithm method of ground-air infrared detection range. *Electro-Opt. Technol. Appl.* **2009**, *24*, 29–32.
26. Zhang, J.; Fang, X. *Infrared Physics*; Xidian University Press: Xi'an, China, 2004.
27. Liu, L.; Dong, S.; Yu, Q.; Tan, H. Atmospheric mean transmittance in wavelength interval 0.1 μm from infrared 1 to 14 μm , (II) transmittance of water vapor. *J. Harbin Inst. Technol.* **1999**, *6*, 75–78.
28. Liu, L.; Dong, S.; Yu, Q.; Tan, H. Atmospheric mean transmittance in wavelength interval 0.1 μm from infrared 1 to 14 μm (II) transmittance of carbon dioxide. *J. Harbin Inst. Technol.* **1998**, *5*, 9–13.
29. Lu, Y. Simple method to calculate the atmosphere transmittance of infrared radiation on slanting route. *Infrared Laser Eng.* **2007**, *4* (Suppl. S2), 423–426.
30. Li, N.; Yang, C. Radiation calibration for 3–5 μm infrared detector. *Infrared Laser Eng.* **2012**, *41*, 858–864.
31. Liu, B.; Zheng, W.; Li, H. Research progress in measurement technology of material surface emissivity. *Infrared Technol.* **2018**, *40*, 725–732.
32. Wang, Z.; Liu, Z.; Xia, X. *Measurement Error and Uncertainty Evaluation*; Science Press: Beijing, China, 2008.
33. Sun, Z.; Wu, H.; Yuan, W.; Wen, Z. *Calculation Method and Practice*; Southeast University Press: Nanjing, China, 2011.
34. Pierce, A.K.; Allen, R.G. The Solar Spectrum Between 0.3 and 10 μm . In *The Solar Output and Its Variation*; Colorado Associated University Press: Boulder, CO, USA, 1977.
35. Jursa, A.S. *Handbook of Geophysics and the Space Environment*, 4th ed.; Air Force Systems Command; U.S. Department of Commerce National Technical Information Service: Springfield, VA, USA, 1985.
36. Yuan, Z. The effect and correction of blackbody radiation emissivity on the accuracy for radiation thermometry. *Acta Metrol. Sin.* **2007**, *28*, 19–22.
37. Ma, J.; Wen, M. Skin Radiation Measurement Method of High Altitude Aircraft Based on Long Wave Infrared Light. *Infrared Technol.* **2021**, *43*, 284–291.